Designing a Hydrophobic Barrier within Biomimetic Nanopores

Jemma. L. Trick,[†] E. Jayne Wallace,[‡] Hagan Bayley,[§] and Mark. S. P. Sansom*,[†]

[†]Department of Biochemistry, University of Oxford, South Parks Road, Oxford OX1 3QU, Oxford, United Kingdom, [‡]Oxford Nanopore Technologies Ltd., Edmund Cartwright House, 4 Robert Robinson Avenue, Oxford Science Park, Oxford OX4 4GA, Oxford, United Kingdom, and [§]Chemistry Research Laboratory, University of Oxford, 12 Mansfield Road, Oxford OX1 3TA, Oxford, United Kingdom

ABSTRACT Nanopores in membranes have a range of potential applications. Biomimetic design of nanopores aims to mimic key functions of biological pores within a stable template structure. Molecular dynamics simulations have been used to test whether a simple β-barrel protein nanopore can be modified to incorporate a hydrophobic barrier to permeation. Simulations have been used to evaluate functional properties of such nanopores, using water flux as a proxy for ionic conductance. The behavior of these model pores has been characterized as a function of pore size and of the hydrophobicity of the amino acid side chains lining the narrow central constriction of the pore. Potential of mean force calculations have been used to calculate free energy landscapes for water and for ion permeation in selected models. These studies demonstrate that a hydrophobic barrier can indeed be designed into a β-barrel protein nanopore, and that the height of the barrier can be adjusted by modifying the number of consecutive rings of hydrophobic side chains. A hydrophobic barrier prevents both water and ion permeation even though the pore is sterically unoccluded. These results both provide insights into the nature of hydrophobic gating in biological pores and channels, and furthermore demonstrate that simple design features may be computationally transplanted into β-barrel membrane proteins to generate functionally complex nanopores.
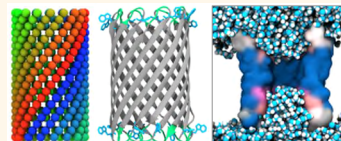
KEYWORDS: biomimetic pores · molecular dynamics · simulations · computational modeling

Nanopores in membranes have a wide range of potential applications, including biosensors,[1,2] nanoreactors for single molecule chemistry,[3] desalination of water, and within DNA sequencing devices.[4−6] Such pores may be derived from existing biological (protein) nanopores,[7−9] may be formed by stacks of synthetic cyclic peptides,[10,11] or may be non-biological pores formed within, *e.g.*, polymer membranes,[12] based on graphene sheets[13,14] or carbon nanotubes,[15] as discussed in a recent review.[16] More recently, novel nanopores have been designed by DNA origami.[17,18]

In designing nanopores, one approach is to mimic key features of biological nanopores (*e.g.*, ion channels and bacterial porins) of known structure and function. Bacterial porins provide a range of conductances and selectivities to inorganic ions, and also to other solutes such as sugars and antibiotics.[19−23] Furthermore, porins show high stability to unfolding[24] so are generally stable over a wide range of temperatures and perturbing conditions.

Thus, porins and related outer membrane proteins from Gram-negative bacteria have

the potential both to provide design motifs for biomimetic nanopores and to act as templates for generation of functional pores. A recent example of this approach is provided by the phosphate selective porin OprP (pdb: 2O4V).[25] With the analysis of the physico-chemical principles underlying phosphate selectivity computationally,[26,27] it was possible to design simple model nanopores *in silico*, which mimicked the free energy landscapes for anion permeation of the parent protein. There have also been a number of studies to help define ungated and nonselective "bland" β-barrel pores, which might act as templates for nanopore design. These have included the simple porin OmpG.[9] In the latter case, simulations were used to aid design of a silent version of the OmpG pore which did not exhibit significant gating activity.

Molecular dynamics (MD) simulations play a key role in allowing us to understand the physical basis of nanopore function, both for biological pores such as general porins,[28,29] OpdK,[30] OmpF,[31] α-HL,[32−34] for models based on, *e.g.*, carbon nanotubes[35,36] and for theoretical models,[37,38] with simulations

©2014 American Chemical Society

being used to explore more general models of pore selectivity and gating. For example, simulations of simple model nanopores have been used to define and explore the concept of hydrophobic gating[39,40] (sometimes conceptualized as the formation of nanoscopic bubbles)[41] whereby a narrow hydrophobic region excludes water and ions, and hence may functionally close a pore that, however, is not sterically occluded.

A number of studies, both computational and experimental, have suggested that hydrophobic gating may occur in certain ion channel proteins including the mechanosensitive channel MscL,[42−44] the nicotinic acetylcholine receptor,[45,46] its bacterial homologues,[47] and voltage gated potassium channels,[48] as reviewed recently.[49] More recently, experimental studies have demonstrated the feasibility of designing hydrophobic gates into nonbiological nanopores[50] and have revealed the presence of a hydrophobic barrier deep within the pore of the TWIK-1 potassium channel.[51] It is thus of interest to explore whether simulations can be used to design a hydrophobic barrier within a nanopore based on a β-barrel protein template.

To design a biomimetic pore, we may wish to transplant a key structural and functional feature from a more complex ion channel into a simple β-barrel template. For example, a hydrophobic gate has not been found in a wide, high conductance β-barrel nanopore. (A hydrophobic pore in a β-barrel is seen in OmpW,[52] but this is very narrow and binds detergent molecules.) Therefore, we wish to test whether a hydrophobic barrier formed by consecutive rings of hydrophobic side chains in the pore lining (as seen in the nicotinic acetylcholine receptor and related channels)[53] can be designed into a bland high conductance β-barrel in order to control the conductance of the resultant nanopore.

In the current study, we design β-barrel nanopores that contain a hydrophobic barrier. We use MD simulations to explore the function of such nanopores, initially using water flux as a proxy for ionic conductance. We explore the behavior of these pores as a function of the size (in terms of number of strands) and hydrophobicity of the amino acid side chains forming the hydrophobic barrier. Finally, potential of mean force (PMF) calculations are used to reveal the energy landscapes that define water and ion permeation. These studies provide a detailed example of the use of MD simulation to design and evaluate simple model nanopores based on a β-barrel template, with a prospect of their further development for biotechnological applications.

RESULTS AND DISCUSSION

Modeling β-Barrel Nanopores. On the basis of detailed visual inspection of the known structures of bacterial β-barrel membrane proteins, we set out to design
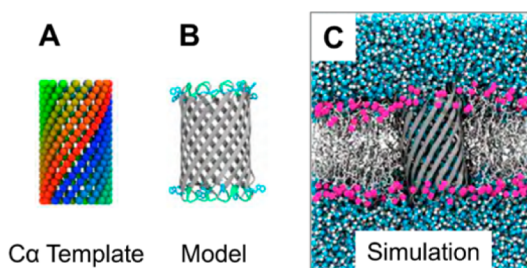

Figure 1. Overview of nanopore modeling and simulations. (A) Cα representation of the idealized peptide backbone template for a 16 stranded antiparallel β-barrel with a barrel shear number S = 16. (B) A β-barrel nanopore model built using the template shown in A. The protein model is shown with the β-strands in gray, glycine-containing loops in green, and tryptophan anchor residues in blue. (C) Snapshot from a MD simulation of the β-barrel nanopore model embedded in a DPPC bilayer (acyl tails in gray, phosphate groups in pink) with surrounding water molecules in blue/white van der Waals representation (ions are not shown for clarity).

biomimetic model nanopores with 12, 14, or 16 strands per β-barrel. Such pores are seen within naturally occurring β-barrel proteins, for example the porin NanC (pdb: 2WJQ),[54] which has 12 strands, and the toxins α-hemolysin (pdb: 7AHL)[55] and γ-hemolysin (pdb: 3B07),[56] which contain 14 and 16 β-strands, respectively.

To generate and evaluate these models, we used the workflow illustrated in Figure 1. The initial Cα template was generated based on the idealized geometry of a transmembrane β-barrel.[57] The strand lengths (of 20 residues) were set to generate nanopores of length 40−42 Å, sufficient to span a lipid bilayer. These templates were converted to protein models using MODELER[58] and then embedded in a simple phospholipid bilayer for evaluation in terms of stability and permeation properties by atomistic MD simulations.

To generate minimalist biomimetic β-barrel nanopores, which would sit stably within a lipid bilayer, the outer surface of the barrel was covered with hydrophobic leucine side chains. The β-strands were connected by short flexible loops compromising of glycine residues (ca. 2 to 3 residues). A band of tryptophan residues was included on the outer surface at each end of the barrel, as the amphipathic aromatic tryptophan side chains are known to "lock" membrane proteins into place in a lipid bilayer by forming hydrogen bonds to lipid headgroups.[59,60] Together these features were designed to form a stable transbilayer nanopore, allowing the nature of the inward facing pore-lining side chains to be designed in order to control water and ion permeation. (The design of the specific nanopore sequence to generate such templates is described in more detail in the Materials and Methods and Supporting Information Figure S1).

To evaluate these models, atomistic MD simulations (of duration from 40 to 100 ns, see Table 1) were performed of the nanopore embedded in a DPPC

TABLE 1. Summary of Models and Simulations

N	Shape	Pore lining rings[a]	Time (ns)	Cα RMSD (Å)	Minimum radius (Å)	Mean water flux (ns⁻¹)
12	F	GGAAVVL	100	4.6	1.0	0.1
		SSTTNNQ	100	3.6	3.2	13
12	HG	GAVLVAG	100	4.5	1.0	0.1
		GAVQVAG	2 x 40	5.1	1.6	3.0
		STNQNTS	100	5.0	3.3	13
		STNFNTS	40	3.8	2.9	12
		STNLNTS	40	5.5	3.9	18
14	F	GGAAVVL	2 x 100	3.7	4.9	0.2
		SSTTNNQ	100	3.5	4.5	29
14	HG	GAVLVAG	3 x 100	4.1	4.5	0.4
		GAVQVAG	3 x 40	3.8	4.4	35
		STNQNTS	2 x 100	3.7	4.5	32
		STNFNTS	40	4.3	4.0	26
		STNINTS	40	3.2	5.1	34
		STNLNTS	100	4.2	5.2	37
		STNWNTS	40	3.4	3.2	23
		STNYNTS	40	3.8	2.6	12
		TNLLLNT	100	3.8	5.5	0.5
		TNNLLNT	100	5.1	5.1	34
		STNIINT	100	4.3	5.4	45
		STLLLTS	2 x 100; & 40	4.7	5.4	0.3
		STNLLTS	3 x 100; & 40	4.8	5.1	26
		STNLLNT	3 x 100	4.1	5.2	23
16	F	GGAAVVL	100	4.7	6.3	80
		SSTTNNQ	100	3.9	4.8	50
16	HG	GAVLVAG	100	4.1	4.6	55
		STNQNTS	2 x 100	4.2	6.2	64
		STNFNTS	40	4.4	6.3	63
		STNLNTS	40	3.8	7.1	61
		STNWNTS	40	3.4	5.2	48
		STNYNTS	40	3.6	5.8	51

[a] The rings of pore-lining residues are listed, with residues colored based on their polarity/hydrophobicity as in the figures: blue = hydrophobic; pink = hydrophilic; W and Y in purple.

bilayer with a 1 M NaCl solution on either side of the bilayer. Models were assessed in terms of conformational stability of the protein, dimensions of the transbilayer pore, and the flow of water and ions through the pore.

Design Principles. In our initial exploration of possible designs, we explored both funnel (F) and hourglass (HG) shaped pores (Figure 2A). The latter have a central constriction that mimics porins more closely, as many porins also have a central constriction.[61−63] The overall size of the nanopores was determined by the number of strands in the barrel (12, 14, or 16; see above) while the shape (F or HG) was determined by the sizes of the residues lining the pore. The nature of the pore-lining side chains was varied to yield either a hydrophobic (lined by Gly, Ala, Val, and Leu residues; Figure 2B) or hydrophilic (lined by Ser, Thr, Asn, and Gln) pore. Thus, each pore design may be described by the number of β-strands in the barrel template, the overall shape of the pore, and by specification of the rings of side chains

lining the pore. Examples of two such pore models (N = 14, F, SSTTNNQ and N = 14, HG, STNQNTS) and the resultant pore lining surfaces (as evaluated using HOLE)[64] are shown in Figure 2C.

The overall conformational stability of these pore models was evaluated by measurement of the RMSD from the initial model over the course of the atomistic MD simulation. For example, for the N = 14, HG STNQNTS model, the overall Cα RMSD (Supporting Information Figure S2; all residues) plateaus at ca. 4 Å, just a little higher than would be the case for comparable simulations of native porin structures.[28,65] The conformational fluctuations are higher for the interstrand loops, again as expected (Supporting Information Figure S2C). Thus, the de novo designed nanopores behave in a similar manner to porins in MD simulations in a bilayer on a ca. 100 ns time scale. Calculation of the pore radius profile at selected time points during the simulation suggests that the initial model structure of the pore "relaxes" to adopt a more
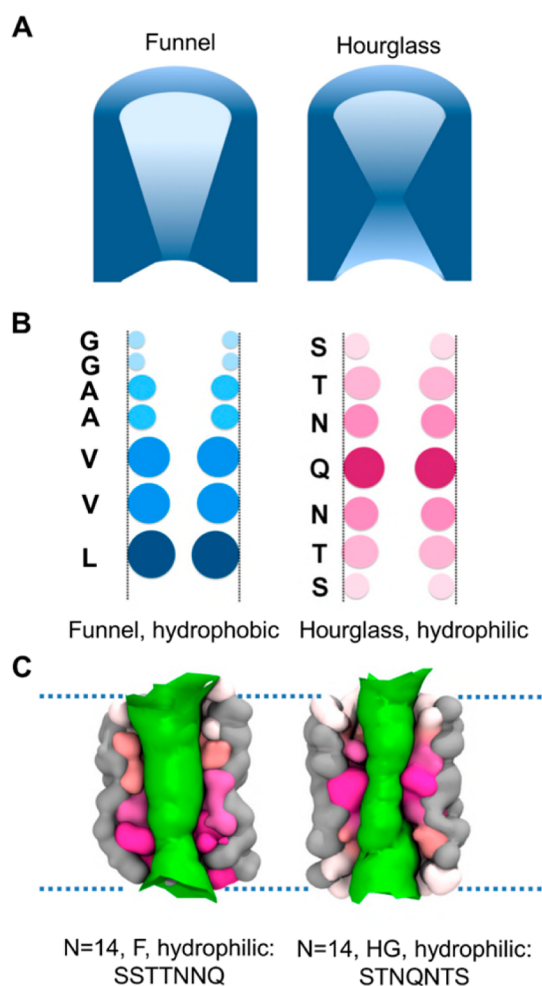
Figure 2. Design of nanopores, from concept to model. (A) Design of the shape of a nanopore, showing funnel or hourglass shaped pores. (B) Implementation of the design based on the sizes of the side chains lining the pore (Supporting Information Figure S1 for further details of the protein sequence). Representations of a hydrophobic funnel-shaped pore and a hydrophilic hourglass-shaped pore are shown. The color code is pink for hydrophilic pore-lining side chains and blue for hydrophobic, with the gradient from pale to dark indicating increasing size of the residue side chain. (C) Space filling models (with the pore-lining surface as defined by HOLE[64] in green) of funnel shaped (F) and hourglass shaped (HG) hydrophilic $N = 14$ β-barrel pores, with the pore lining rings of polar side chains (STNQNTS) shown using the same pink scale as in B and the surrounding β-barrel in gray.

Figure 3. Three generations of designs of β-barrel nanopores. The flow diagram indicates the evolution of the designs in terms of number of β-stands (N), shape (hourglass HG vs funnel F) and the nature of the pore-lining residues (shown using the same color scheme as in Figure 2B).

clearly hourglass shape, with a shift in the minimum radius at the central constriction from *ca.* 3 to *ca.* 4 Å over the duration of the simulation. Comparable changes in pore radius profiles have also been seen in simulations of porins[66,67] and confirm the importance of relaxing initial pore models by MD simulation before evaluating them in terms of pore radius and permeability properties.

Having established an overall methodology, we used this to explore three generations of nanopore design, as summarized in Figure 3. The first generation, as described above, provided an overall exploration of
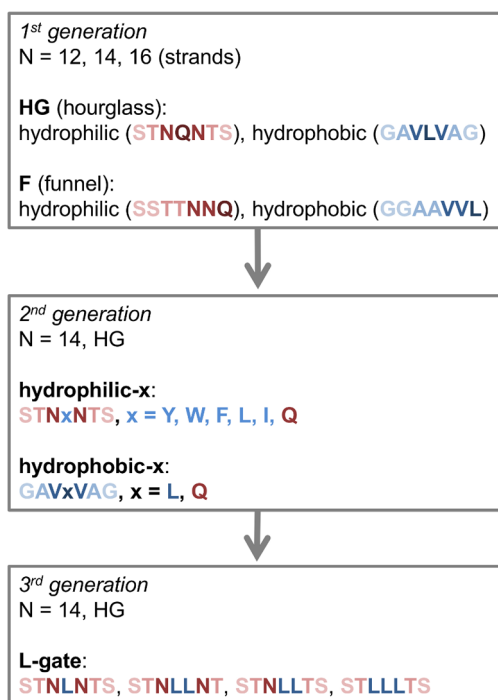
pore size, shape, and hydrophobicity of the pore lining residues. The second generation models explored further refinements of the stable $N = 14$, HG first generation models. Thus, both $N = 14$, HG STNQNTS and $N = 14$, HG GAVLVAG were used as "host" pores for a central ring of "guest" residues, yielding the hydrophilic-x and hydrophobic-x models, respectively (Figure 3). This involved the replacement of the central, constricting residues of either the hydrophobic or hydrophilic pore with the opposite type of residue. So, *e.g.*, a hydrophobic residue, L (Leu), was introduced into the central ring of the hydrophilic STNQNTS pore or a hydrophilic residue, Q (Gln), was introduced into the central ring of the otherwise hydrophobic GAVLVAG pore.

In the third generation of models, $N = 14$, HG models were explored further, combining an overall hydrophilic pore lining with 1, 2, or 3 rings of L side chains to yield a central hydrophobic constriction of increasing thickness.

Water Flux through First Generation Models of β-Barrel Nanopores. We first examined water flux as a proxy for ionic conductance, *i.e.*, as a simple measure of pore "openness". This was analyzed because time scales for ion conduction would require substantially longer simulation times in order to detect significant differences in conductance[39] through members of the first generation of pore models. If we focus on the $N = 12$, 14, and 16 HG hydrophilic pores, we can see that each model retains the hourglass shape over the course of

the simulations (Figure 4A), with minimum radii ranging from *ca.* 3 Å ($N = 12$) to *ca.* 6 Å ($N = 16$), and water fluxes ranging from *ca.* 13 ns^{-1} ($N = 12$) to *ca.* 64 ns^{-1} ($N = 16$). Thus, as might be anticipated from simple geometric considerations, the water flux scales with the minimum cross-sectional area of the pores.

Cumulative water fluxes (either 'upward' or 'downward' dependent on whether the direction of flow is measured in a positive or negative *z* direction; Figure 4B) were evaluated for these three models over the course of the simulations. As noted above the water flux scales approximately with the cross-sectional area of the central constriction of the pore. Extending this analysis to all of the first generation pores (Figure 4C) shows a clear correlation between the cross sectional area of the central constriction and the water flux averaged over the simulation, provided one excludes the $N = 12$ and $N = 14$ hydrophobic pores, which did not conduct water (not shown in figure). Of course, this analysis ignores complexities arising from the overall shape of the pores, which has been suggested to be of importance in, *e.g.*, water flow through aquaporins[68] and which is present in conical nanopores such as MspA.[69]

The hydrophobic funnel shaped pores did not retain a clearly defined radius profile over the course of the simulations (Supporting Information Figure S3). Thus, all three funnel shaped hydrophobic pores occluded to some extent at their mouths, this being clearest for the $N = 12$ pore. Consequently, the $N = 12$ and $N = 14$ pores did not conduct water at a high rate. The $N = 16$ pore remained unoccluded, with an average radius of *ca.* 6 Å. Hence, this pore did conduct water (*ca.* 55 ns^{-1}), albeit at a lower rate than comparable hydrophilic pores.

Water Flux through Second Generation Pore Models. From the simulations of first generation models, we can see that the $N = 14$, HG models form stable pores, which conduct water, but which are sufficiently narrow to be functionally sensitive (in terms of water flux) to the nature (hydrophilic *vs*, hydrophobic) of the pore lining residues (with a flux of 31.9 ns^{-1} for $N = 14$, HG, hydrophilic *vs* 0.4 ns^{-1} for $N = 14$, HG, hydrophobic). Also, in the first generation simulations, the hourglass pores maintained their desired, initial shape more consistently than the funnel shaped pore models (data not shown), and hence, we focus on the HG models from now onward. So, in the second generation of models, we either introduce a central ring of hydrophobic residues into a hydrophilic HG pore (by replacement of the central glutamine ring by a hydrophobic residue X to give the hydrophilic-*x* models; see Figure 3), or we incorporate a central ring of glutamine residues into the hydrophobic HG pore, to give a hydrophobic-Q model.

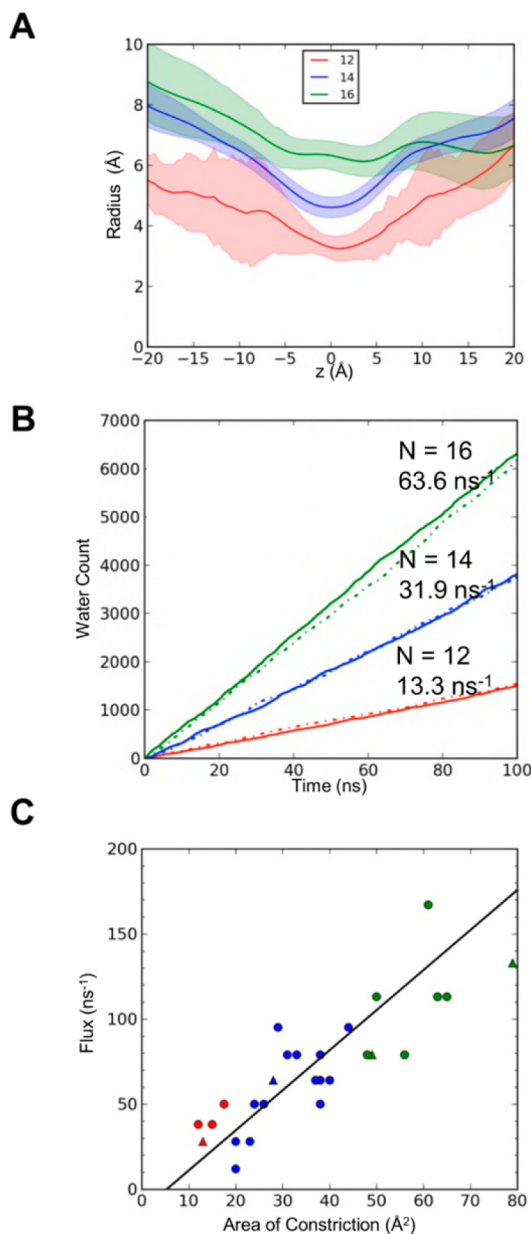It is instructive to compare in detail the hydrophobic-L and -Q models (Figure 5) in which the central

Figure 4. Water flux through first generation models of β-barrel nanopores. (A) Pore radius profiles (calculated using HOLE) for the first generation $N = 12$, 14, and 16 hydrophilic hourglass model pores. The profiles shown are the averages across 100 ns MD simulations of the pores in a bilayer, where the shaded region corresponds to the standard deviation of the RMSD of the pore throughout the simulation. (B) Cumulative water fluxes (solid lines indicate "upward" and broken lines "downward" flux with respect to the protein and the simulation box) for the $N = 12$, 14, and 16 pores in A. The slopes of the lines correspond to water fluxes of 13.3, 31.9, and 63.3 ns^{-1} for the $N = 12$, 14, and 16 pores, respectively. (C) Relationship between the water flux rate (averaged in each case over a 100 ns simulation) and the cross-sectional area at the pore constriction. Points are shown for $N = 12$ (red), 14 (blue), and 16 (green) models, with circles corresponding to HG and triangles to F shaped pores. Hydrophobic pores are not shown.

leucine constriction is replaced by a glutamine ring. The pore radius profiles of the two models are very similar. The hydrophobic-Q model has a constriction
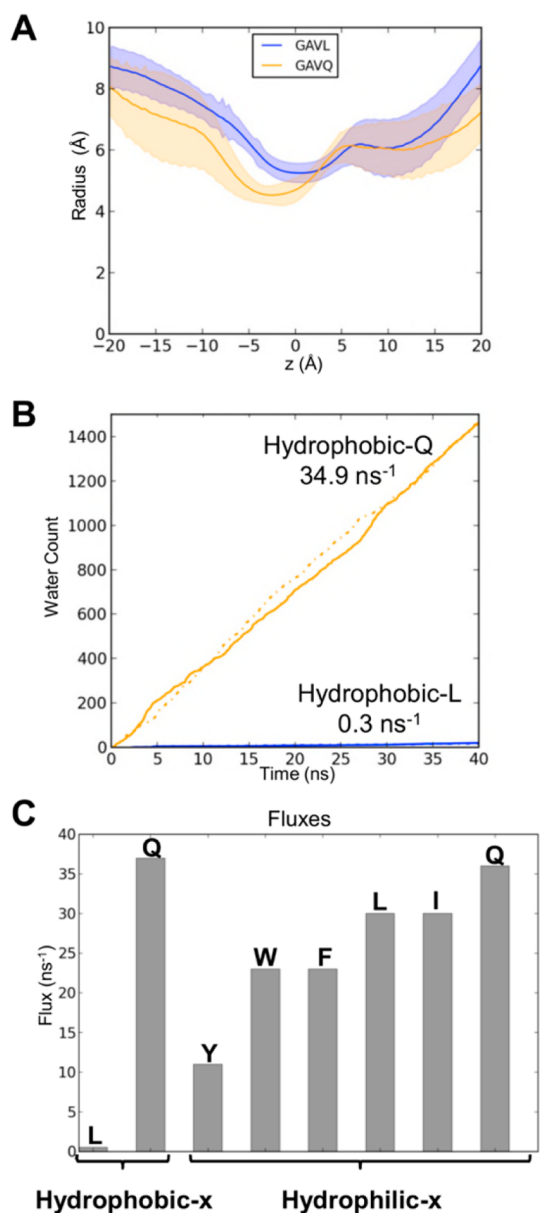
Figure 5. Water flux through second generation pore models. (A) Pore radius profiles through the second $N = 14$, HG, hydrophobic-X pore models, where X = L (blue) or Q (orange). (B) Cumulative water fluxes (solid lines "upward" and broken lines "downward") for the $N = 14$ hydrophobic-L (blue) and hydrophobic-Q (orange) pores in A. The slopes of the lines correspond to water fluxes of 0.4 and 34.9 ns^{-1} for the hydrophobic-L and hydrophobic-Q pores, respectively. (C) Water fluxes for the hydrophobic-X and hydrophilic-X pores shown as a function of the central constriction side chain residue 'X' depicted in Figure 3.

radius of 4.5 Å, which is slightly smaller than that of the hydrophobic-L model. However, replacement of the leucine ring at the constriction by the glutamine ring leads to a nearly 40-fold increase in water conductance (Figure 5B and Supporting Information Figure S4). We note that the conductance of the hydrophobic-L pore at 1 ns^{-1} is less than that of the single file conductance of water (ca. 3 ns^{-1}) in the (ion impermeable) aquaporins.[70] Thus, introduction of a single Gln ring

into the constriction of an otherwise hydrophobic pore has enabled the hydrophobic barrier to be breached. This reflects the ability of polar (H-bonding) side chains to stabilize water within a hydrophobic barrier region as demonstrated both in earlier simulation studies of simple models of nanopores[39] and in more recent combined experimental and computations studies of TWIK-1 potassium channels.[51]

We also examined a series of hydrophilic-X models (Figure 5C) in which a central hydrophobic ring was introduced into a hydrophilic HG pore. All of the hydrophilic-X pores showed significant water conductance. However, there was a graded reduction observed as the size of the residues forming the hydrophobic constriction ring was increased. It is interesting to note that there is a greater increased conductance in the hydrophilic-W model than in the smaller hydrophilic-Y pore, even though the W (tryptophan) side chain is larger than the Y (tyrosine). This seemed to reflect a change in conformation via rotation of the smaller Y side chains, which resulted in local pore deformation, thus resulting in a narrower pore and a smaller water flux.

On the basis of these second generation models, we can see that the functional "openness" of the pores can be successfully modulated by changing the nature of the central constriction, and that this is most sensitive when a central hydrophobic barrier is placed in a hydrophilic pore background. This was then explored in further detail in the third generation models.

Hydrophobic Barriers within the L-Gate Designs. The second generation hydrophilic-X models (see above) revealed that introducing a single ring of leucines into the center of the pore was not sufficient to functionally close the pore. Therefore, in the third generation L-gate models (see Figure 3), we examined the effect of increasing the thickness of the central hydrophobic constriction by introducing either two or three rings of leucines to give the STNLLNT, STNLLTS, and STLLLTS models.

Each of these models has a minimum radius of ca. 5.5–6 Å (Supporting Information Figure S5B). We note that this radius is comparable to that which resulted in hydrophobic gating (see as dynamic dewetting) of simplified models of nanopores.[39] Significantly, for all three models, dynamic wetting/dewetting is observed within our simulations, seen as stochastic steps in the cumulative water flux curves (Figure 6). Visualization of the simulations reveals that, as anticipated, the dewetting occurs in the vicinity of the central rings of hydrophobic side chains. In terms of water conductance this ranges from ca. 30 ns^{-1} for the STNLLTS pore to 0.2 ns^{-1} for the STLLLTS pore. We note that in the latter case this is an order of magnitude smaller than the experimentally observed single file water conductance of aquaporin.[70] The amphipathic pore of aquaporin is continuously occupied by water and so does not exhibit dewetting.
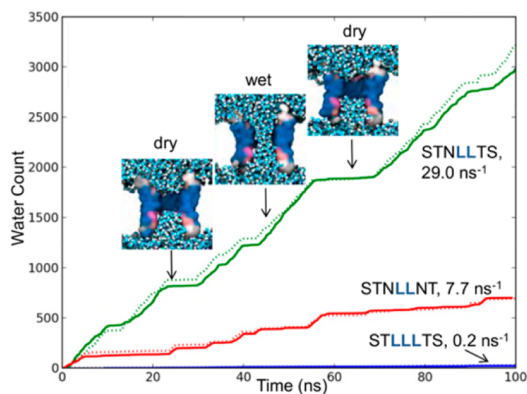
Figure 6. A hydrophobic barrier in third generation pore models. Cumulative water fluxes (solid lines "upward" and broken lines "downward") for the $N = 14$, HG L-gate pores. The inset images show three snapshots from the simulation of the STNLLTS pore, illustrating stochastic wetting and drying of the hydrophobic barrier region (barrier shown in gray, the water molecules are shown in blue/white). The small vertical arrows show the corresponding points on the water flux curve. Average flux indicated on figure.

So far we have only measured water conductance through these model pores, considering this as a proxy for ionic conductance. We initiated our explorations of the behavior of ions within our models of hydrophobic pores by taking a dewetted state from a simulation of, *e.g.*, the STNLLNT model, and restraining a Cl$^-$ ion in the region of the central constriction (Supporting Information Figure S6). While the ion was restrained in this position, it resulted in persistent wetting of the central region of the pore. However, upon removing the restraint on the ion, the ion was quickly expelled from the central region of the pore, leading to pore dewetting. This suggests that the dewetted state of the channel in the absence of an ion is more stable and, hence, that the channel is functionally closed. However, this observation also argues for a more detailed analysis of the energy landscapes of water and ion permeation through these perhaps surprisingly complex model nanopores.

Energy Landscapes for Permeation: Water and Ions. One approach to understanding the nature of a hydrophobic gate is to characterize the free energy landscape of permeation in the presence of such a barrier. To this end, we have determined potentials of mean force (PMF) for translation of a single water molecule or of a chloride ion along the pore axis for the three third generation model pores (Figure 7). Considering first the water PMFs (Figure 7A), we can see, as anticipated, a clear correlation between the height of the central energy barrier and the rate of water flux seen in the 100 ns simulations.

Thus, the barrier height is *ca.* 24 kJ mol^{-1} for the STLLLTS model, which in equilibrium simulations exhibited a very low conductance for water. In contrast, the two models with a double ring of leucine residues at the central constriction, which showed a higher
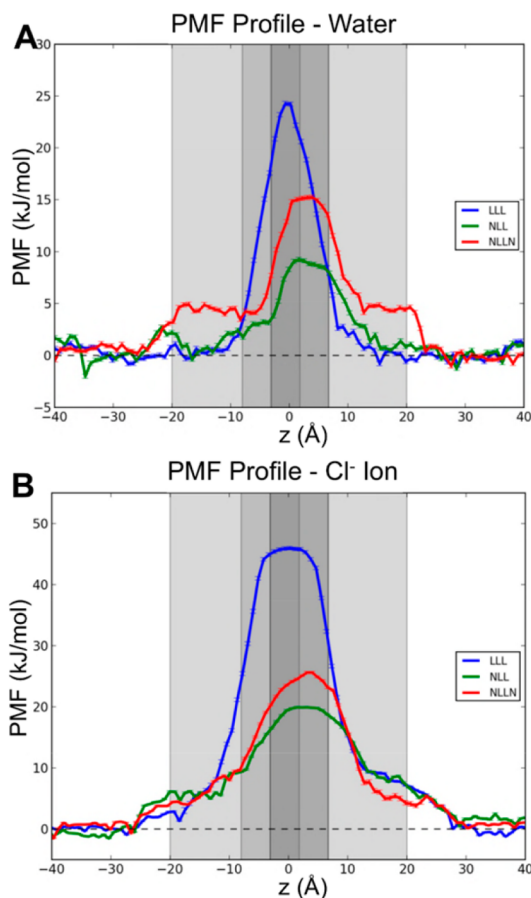

Figure 7. (A) Potentials of mean force (PMF) calculations for a water molecule along the three $N = 14$, HG L-gate pores. The reaction coordinate corresponds to the z coordinates of the water (oxygen atom) relative to the center of mass of the pore. The protein spans from $z = -20$ to $+20$ Å (light gray) with darker gray panels showing the hydrophobic barrier region, *i.e.*, NLL or LLL for all models. The second and third leucines are represented by the darkest gray panel. **(B)** The corresponding PMFs for a Cl$^-$ ion along the same pores as in A.

water conductance, had smaller free energy barriers: *ca.* 9 kJ mol^{-1} for STNLLTS and *ca.* 15 kJ mol^{-1} for STNLLNT. The shape of the barrier also correlates well with the positions of the hydrophobic rings occurring at the center of the pore for the STLLLTS model but being slightly displaced to positive z values for the STNLLST and STNLLNT models as they are asymmetric.

The PMFs for chloride ions (Figure 7B) show a similar behavior. Thus, the STLLLTS model has a barrier for chloride of *ca.* 46 kJ mol^{-1} in contrast to a barrier height of *ca.* 26 kJ mol^{-1} for the STNLLNT and *ca.* 20 kJ mol^{-1} for STNLLNT models. This is encouraging as it suggests water permeation may indeed be used as a proxy for ion permeation in designing hydrophobic gates or barriers into nanopores. However, we note that the barriers are substantially higher for ions than they are for water, as has been seen for simple models of nanopores,[71] for gramicidin A,[72] and for the nicotinic acetylcholine receptor.[45] A PMF was also calculated for a sodium ion in the STLLLTS pore. Comparison of the three free
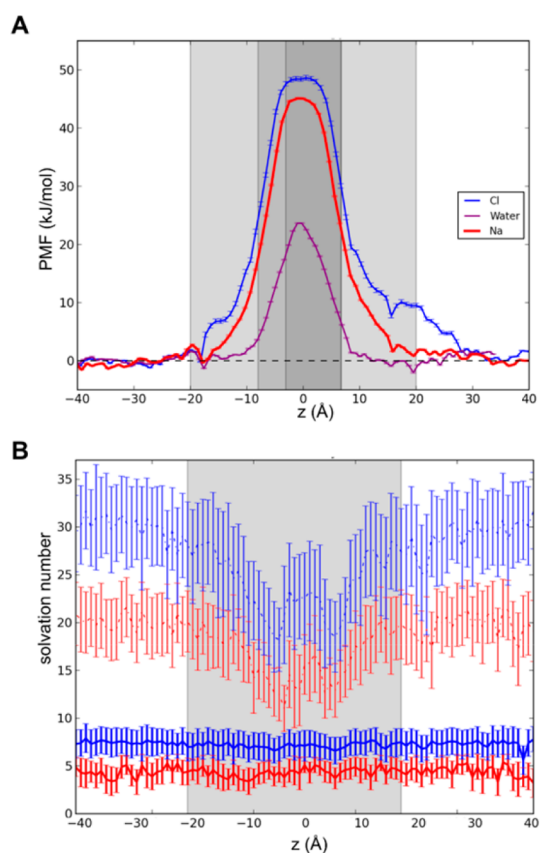
Figure 8. (A) Potentials of mean force (PMFs) calculations for a water molecule (purple), a Cl^- ion (blue) or a Na^+ ion (red) along the three $N = 14$, HG L-gate LLL pore (see main text and Figure 7B for details). (B) Solvation numbers for Cl^- (blue) and for Na^+ (red), using distances cutoffs of 4.0 Å for the inner shell (thick lines) and 6.3 Å for the second shell (thin lines) for Cl^-, and of 3.1 Å for the inner shell and 5.4 Å for the second shell for Na^+.

energy profiles for the STLLLTS model shows those for Cl^- and Na^+ ions to be broadly similar, both with a higher and wider barrier than that for water (Figure 8A).

The origin of the energetic barriers in the PMFs may be further elucidated by calculating the solvation numbers, based on numbers of water−ion contacts within a given cutoff formed by Cl^- and by Na^+ as a function of position along the pore axis during the simulations on which the PMF calculations were based (Figure 8B). From these it can be seen that for ions the first solvation shell remains intact. In contrast, significant depletion of the second solvation shell occurs as the ion passes through the hydrophobic constriction. This suggests that the energetic barrier may reflect largely the cost of hydration of the hydrophobic constriction (as evidenced by the water PMF) plus the cost of removal of (part of) the second hydration shell. We note that a study of the GLIC channel suggested that the barrier to Na^+ permeation presented by the hydrophobic gate arises largely from the cost of hydrating the pore.[73] A similar analysis has been presented for anions passing through simple models of narrow hydrophobic nanopores.[74]

The nanopore PMFs may be compared with those for a model (based on a relatively low resolution structure) of the closed state of the nicotinic acetylcholine receptor (nAChR).[45] For the nAChR M2 helix bundle model, the barriers were of the order of: water 5 kJ mol^{-1}; chloride 15 kJ mol^{-1}; and sodium 25 kJ mol^{-1}. These are somewhat lower barriers than those for our hydrophobic barrier nanopores, reflecting that the nAChR is a more polar pore overall with a single hydrophobic ring of Leu side chains at position 9′ of the M2 helices forming the central barrier. Within the related GLIC channel, the free energy barrier to ion permeation through the pore is estimated to be *ca.* 83 kJ mol^{-1} in the closed state[73] and *ca.* 17 kJ mol^{-1} when the channel is open. These values are higher than our predicted value for sodium translocation through the hydrophobic STLLLTS pore. This could be accounted for by the radius at position 9′ on M2 of GLIC, which is approximately 1.7 Å.

Comparison of the PMFs for water and for ions also allows us to reflect on whether one might use water permeation as a (computationally cheaper) proxy for ionic conductance in filtering out designs based on the former. For the STLLLTS model, it is evident that the energetic barriers for ions are higher than those for water (see above), so a conclusion that the pore would be functionally closed based on the water permeation alone would be correct. However, to check this approach further, we went back to the second generation hydrophobic-X pores (see Figure 5 and above). On the basis of water flux, we had judged the hydrophobic-Q pore (water flux 35 ns^{-1}) to be open while the hydrophobic-L pore was closed (water flux 0.3 ns^{-1}). Calculation of Cl^- ion PMFs for these two models (Supporting Information Figure S7) revealed a relatively flat permeation profile with a central minimum for the hydrophobic-Q pore in contrast to a barrier of +60 kJ mol^{-1} for the hydrophobic-L pore. Thus, it would seem that using calculations of water fluxes as an initial screen of models is a reasonable approximation.

CONCLUSIONS

We have computationally transplanted a hydrophobic barrier (derived from gating mechanisms in the nicotinic acetylcholine receptor and in the bacterial MscS mechanosensitive channel)[45,75] into a family of simple model protein nanopores based on porin-like transmembrane β-barrels. The designed nanopores mimic the template proteins in terms of overall nanopore stability in *ca.* 100 ns MD simulations in a simple phospholipid bilayer. Using these models, we have investigated the effect of size, shape, and of the hydrophobicity/hydrophilicty of the pore lining on water flux through the nanopores (in part using water as a proxy for ionic currents). A number of clear trends emerged, in particular the generation of a hydrophobic barrier (along with associated stochastic wetting/dewetting

behavior)[76,77] when a central constriction lined by successive rings of leucine residues is engineered into the pore. More detailed analysis of permeation free energy landscapes, for water and for monovalent ions, reveals that the height of the energetic barrier associated with the hydrophobic barrier can be engineered by modifying the number of successive rings of leucine residues. This provides both insights into the fundamental properties of hydrophobic gating in native channels, and also confirms that simple design features such as a hydrophobic barrier may be computationally transplanted into β-barrel nanopores, which could be used to create a lower conductance pore. To form a hydrophobic gate, such a barrier has to be switchable between a closed and an open state. For example, one might attempt to transplant a pH sensitive hydrophobic gate based on the ring of histidine side chains present in the proton-activated M2 channel of influenza A.[78]

Three experimentally testable predictions emerge from this computational study. The first is that water permeability is determined by the water free energy barrier height, and will vary by about 2 orders of magnitude across the L-gate models from STLLLTS (ca. 0.2 ns^{-1}) to STNLLTS (ca. 30 ns^{-1}). Such a difference should be measurable, if the corresponding protein nanopores can be generated experimentally and inserted into a lipid bilayer. The second experimentally testable prediction concerns the barrier to ion permeation presented by such hydrophobic gates. We would predict (based on, e.g., simulations of single file water in simple nanopores)[76,77] that application of a sufficiently high voltage across a hydrophobic barrier in a nanopore would lead to voltage dependent wetting and functional opening of the pore. Indeed, such voltage-dependent wetting has been observed for nonprotein nanopores with hydrophobic linings, both in SiN$_3$[79] and in track etched nanopores in PET membranes.[50] It is possible to explore voltage-dependent wetting by simulation, using 'computational electrophysiology' whereby an ionic concentration gradient is used to impose a voltage difference across a membrane.[80] Thus, by combining experimental and computational methods it should prove possible to define the magnitude of the voltage needed to wet (and thereby open) closed pores with differing hydrophobic barrier heights. It should be noted that such simulations are relatively computationally expensive and so are not (currently) well suited to initial screening of possible models. A third experimentally testable prediction concerns the hydrophobic-L and hydrophobic-Q pores discussed above. These differ simply in the nature of the central constriction (L vs Q), yet on the basis of both of their water fluxes and of their Cl$^-$ ion PMFs (Supporting Information Figure S7) would be predicted to show a large difference in conductance.

Inevitably, there are methodological limitations to the current study. In particular, we have not explored the sensitivity of the energy landscape to the water model employed. It could be of interest to examine how the use of polarizable force fields for water and/or protein could allow refinement of the free energy landscape for a nanopore containing a hydrophobic barrier.[81−84] It would also be of interest to explore possible sensitivity to the nature of the lipid bilayer in which the pore is embedded.

There are a number of possible extensions to this work. Having explored the nature of the permeation free energy landscapes for water and for ions, it would be of interest to extend such studies to permeation of small polar and nonpolar solutes. It will also be of technological interest to explore the behavior of "transplanted" hydrophobic gates in a wider range of protein and nonprotein nanopores/templates.

MATERIALS AND METHODS

Model Construction. Atomic coordinates for the $C\alpha$ models were generated using idealized models for transmembrane β barrels,[57] allowing for the mapping of the $C\alpha$ positions of a desired barrel template as a function of number of strands, and shear and length of the barrel. The resultant $C\alpha$ templates were used as inputs for MODELER 9v9[58] in conjunction with designed sequences (see Supporting Information Figure S4) in FASTA format. Pore radius profiles of the resultant models were calculated using HOLE.[64]

Simulation System Preparation. Atomistic models of designed pores were converted to a coarse grained (CG) format using procedures described previously with a locally modified version of the widely used MARTINI Force field.[85] CG MD simulations of duration 1 μs were used to position the nanopores within a bilayer. The pore plus bilayer model at the end of these simulations was converted back to an atomistic system using a standard CG2AT[86] protocol.

Atomistic simulations were performed using GROMACS[87,88] version 4.5.5 (www.gromacs.org) and the GROMOS96 43a1 force field.[89,90] Long range electrostatic interactions were treated with the Particle Mesh Ewald method[91] with a short-range cut off of 1 nm and a Fourier spacing of 0.12 nm. The SPC model was used for water.[92] Simulations were performed in the NPT ensemble with the temperature being maintained at 310 K with a v-rescale thermostat[93] and a coupling constant of τ_t = 0.1 ps. Pressure was maintained semi-isotropically using the Parrinello−Rahman algorithm at 1 bar coupled at τ_p = 1 ps. The time step for integration was 2 fs with bonds constrained using the LINCS algorithm.[94] Analysis was conducted with GROMACS routines, MD Analysis,[95] and locally written code. We performed an initial equilibration of each system for 1 ns during which the protein was restrained. Water flux was calculated by counting water molecules crossing through an xy plane centered on the protein within a 20 Å diameter shell from this center. Water crossings were counted as upward (positive) if parallel to z, downward (negative) if antiparallel. Water fluxes were evaluated over the full length of the simulations. In most cases, this did not lead to a major change in estimated flux compared to evaluating the flux for, e.g., the latter half of the simulation (see Supporting Information Figure S8 for an example). Pore radii with error estimate in simulation was calculated within an add

on of MDAnalysis.[96] Molecular graphic images were produced with visual molecular dynamics (VMD).[97]

Umbrella Sampling Simulations and PMF Calculations. The initial system for the umbrella sampling simulations was obtained from a 60 ns equilibration simulation of the nanopore model in a lipid bilayer. The reaction coordinate was defined as the z-axis (which corresponds approximately to the pore axis), ranging from ± 40 Å with the bilayer center at $z = 0$ Å. This was used to define 80 windows along the z axis, with a distance of 1 Å between successive windows. Water molecules or ions, which overlapped with the probe water molecule or ion, were repositioned by energy minimization before the umbrella sampling. A harmonic biasing potential was applied to the z coordinate of oxygen atom of the water molecule or of the ion with a force constant of 1000 kJ mol^{-1} nm^{-2} (acting on the z coordinate only). Each window was simulated for 2 ns for both ion and water PMFs. Convergence was analyzed in terms of the calculated height of the central barrier as a function of the central time for consecutive 0.1 ns segments extracted from each 2 ns window (see Supporting Information Figure S9 for an example). On this basis, the PMF profiles were judged to have converged after *ca.* 0.5 ns, and the PMFs presented were based on data collected for the last 1.5 ns of each window. PMFs were computed using the weighted histogram analysis method (WHAM).[98] PMF profiles were tethered and errors were calculated as standard deviation by the bootstrapping method.

Supporting Information Available: Additional data analysis and details of the models are provided. This material is available free of charge *via* the Internet at http://pubs.acs.org.

REFERENCES AND NOTES

1. Braha, O.; Walker, B.; Cheley, S.; Kasianowicz, J. J.; Song, L.; Gouaux, J. E.; Bayley, H.; Brahal, O.; Cheleyl, S. Designed Protein Pores as Components for Biosensors. *Chem. Biol.* **1997**, *4*, 497–505.
2. Bayley, H.; Cremer, P. S. Stochastic Sensors Inspired by Biology. *Nature* **2001**, *413*, 226–230.
3. Bayley, H.; Luchian, T.; Shin, S.-H.; Steffensen, M. Single-Molecule Covalent Chemistry in a Protein Nanoreactor. In *Single Molecules and Nanotechnology*; Rigler, R., Vogel, H., Eds.; Springer: Heidelberg, 2008; Vol. 24, pp 251–277.
4. Cherf, G. M.; Lieberman, K. R.; Rashid, H.; Lam, C. E.; Karplus, K.; Akeson, M. Automated Forward and Reverse Ratcheting of DNA in a Nanopore at 5 Å Precision. *Nat. Biotechnol.* **2012**, *30*, 344–348.
5. Manrao, E. A.; Derrington, I. M.; Laszlo, A. H.; Langford, K. W.; Hopper, M. K.; Gillgren, N.; Pavlenok, M.; Niederweis, M.; Gundlach, J. H. Reading DNA at Single-Nucleotide Resolution with a Mutant MspA Nanopore and Phi29 DNA Polymerase. *Nat. Biotechnol.* **2012**, *30*, 349–353.
6. Pennisi, E. Search for Pore-Fection. *Science* **2012**, *336*, 534–537.
7. Howorka, S.; Cheley, S.; Bayley, H. Sequence-Specific Detection of Individual DNA Strands Using Engineered Nanopores. *Nat. Biotechnol.* **2001**, *19*, 636–639.
8. Guan, X.; Gu, L.; Cheley, S.; Braha, O.; Bayley, H. Stochastic Sensing of TNT with a Genetically Engineered Pore. *ChemBioChem* **2005**, *6*, 1875–1881.
9. Chen, M.; Khalid, S.; Sansom, M. S. P.; Bayley, H. Outer Membrane Protein G: Engineering a Quiet Pore for Biosensing. *Proc. Natl. Acad. Sci. U.S.A.* **2008**, *105*, 6272–6277.
10. Ghadiri, M.; Granja, J.; Buehler, L. Artificial Transmembrane Ion Channels from Self-Assembling Peptide Nanotubes. *Nature* **1994**, *369*, 301–304.
11. Clark, T. D.; Kobayashi, K.; Ghadiri, M. R. Covalent Capture and Stabilization of Cylindrical Beta-Sheet Peptide Assemblies. *Chem.—Eur. J.* **1999**, *5*, 782–792.
12. Martin, C. R.; Siwy, Z. S. Chemistry. Learning Nature's Way: Biosensing with Synthetic Nanopores. *Science* **2007**, *317*, 331–332.
13. Merchant, C. A.; Healy, K.; Wanunu, M.; Ray, V.; Peterman, N.; Bartel, J.; Fischbein, M. D.; Venta, K.; Luo, Z.; Johnson, A. T. C.; Drndic, M. DNA Translocation through Graphene Nanopores. *Nano Lett.* **2010**, *10*, 2915–2921.
14. Schneider, G. F.; Kowalczyk, S. W.; Calado, V. E.; Pandraud, G.; Zandbergen, H. W.; Vandersypen, L. M. K.; Dekker, C. DNA Translocation through Graphene Nanopores. *Nano Lett.* **2010**, *10*, 3163–3167.
15. Liu, H.; He, J.; Tang, J.; Liu, H.; Pang, P.; Cao, D.; Krstic, P.; Joseph, S.; Lindsay, S.; Nuckolls, C. Translocation of Single-Stranded DNA through Single-Walled Carbon Nanotubes. *Science* **2010**, *327*, 64–67.
16. Hou, X.; Guo, W.; Jiang, L. Biomimetic Smart Nanopores and Nanochannels. *Chem. Soc. Rev.* **2011**, *40*, 2385–2401.
17. Burns, J. R.; Stulz, E.; Howorka, S. Self-Assembled DNA Nanopores That Span Lipid Bilayers. *Nano Lett.* **2013**, *13*, 2351–2356.
18. Langecker, M.; Arnaut, V.; Martin, T. G.; List, J.; Renner, S.; Mayer, M.; Dietz, H.; Simmel, F. C. Synthetic Lipid Membrane Channels Formed by Designed DNA Nanostructures. *Science* **2012**, *338*, 932–936.
19. Rosenbusch, J. P. Characterization of the Major Envelope Protein from *Escherichia coli*. *J. Biol. Chem.* **1974**, *249*, 8010–8029.
20. Schindler, M.; Rosenbusch, J. Structural Transitions of Porin, Transmembrane Protein. *FEBS Lett.* **1984**, *173*, 85–89.
21. Schenkman, S.; Tsugita, A.; Schwartz, M.; Rosenbusch, J. P. Topology of Phage Lambda Receptor Protein. *J. Biol. Chem.* **1984**, *259*, 7570–7576.
22. Schirmer, T.; Rosenbusch, J. P. Prokaryotic and Eukaryotic Porins. *Curr. Opin. Struct. Biol.* **1991**, *1*, 539–545.
23. Pagès, J.-M.; James, C. E.; Winterhalter, M. The Porin and the Permeating Antibiotic: A Selective Diffusion Barrier in Gram-Negative Bacteria. *Nat. Rev. Microbiol.* **2008**, *6*, 893–903.
24. Moon, C. P.; Zaccai, N. R.; Fleming, P. J.; Gessmann, D.; Fleming, K. G. Membrane Protein Thermodynamic Stability May Serve as the Energy Sink for Sorting in the Periplasm. *Proc. Natl. Acad. Sci. U.S.A.* **2013**, *110*, 4285–4290.
25. Moraes, T. F.; Bains, M.; Hancock, R. E. W.; Strynadka, N. C. J. An Arginine Ladder in OprP Mediates Phosphate-Specific Transfer Across the Outer Membrane. *Nat. Struct. Mol. Biol.* **2007**, *14*, 85–87.
26. Pongprayoon, P.; Beckstein, O.; Wee, C. L.; Sansom, M. S. P. Simulations of Anion Transport through OprP Reveal the Molecular Basis for High Affinity and Selectivity for Phosphate. *Proc. Natl. Acad. Sci. U.S.A.* **2009**, *106*, 21614–21648.
27. Modi, N.; Benz, R.; Hancock, R. E. W.; Kleinekatho, U. Modeling the Ion Selectivity of the Phosphate Specific Channel OprP. *J. Phys. Chem. Lett.* **2012**, *3*, 3639–3645.
28. Watanabe, M.; Rosenbusch, J.; Schirmer, T.; Karplus, M. Computer Simulations of the OmpF Porin from the Outer Membrane of *Escherichia Coli*. *Biophys. J.* **1997**, *72*, 2094–2102.
29. Schirmer, T.; Phale, P. S. Brownian Dynamics Simulation of Ion Flow through Porin Channels. *J. Mol. Biol.* **1999**, *294*, 1159–1167.
30. Wang, Y.; Zhao, X.; Sun, B.; Yu, H.; Huang, X. Molecular Dynamics Simulation Study of the Vanillate Transport Channel of Opdk. *Arch. Biochem. Biophys.* **2012**, *524*, 132–139.
31. Ziervogel, B. K.; Roux, B. The Binding of Antibiotics in OmpF Porin. *Structure* **2013**, *21*, 76–87.
32. Aksimentiev, A.; Schulten, K. Imaging Alpha-Hemolysin with Molecular Dynamics: Ionic Conductance, Osmotic Permeability, and the Electrostatic Potential Map. *Biophys. J.* **2005**, *88*, 3745–3761.

33. Wells, D. B.; Abramkina, V.; Aksimentiev, A. Exploring Transmembrane Transport through Alpha-Hemolysin with Grid-Steered Molecular Dynamics. *J. Chem. Phys.* **2007**, *127*, 125101.

34. Luo, Y.; Egwolf, B.; Walters, D. E. E.; Roux, B. Ion Selectivity of Alpha-Hemolysin with a Beta-Cyclodextrin Adapter. I. Single Ion Potential of Mean Force and Diffusion Coefficient. *J. Phys. Chem. B* **2010**, *114*, 952–958.

35. Garcia-Fandino, R.; Sansom, M. S. P. Designing Biomimetic Pores Based on Carbon Nanotubes. *Proc. Natl. Acad. Sci. U.S.A.* **2012**, *109*, 6939–6944.

36. Corry, B. Water and Ion Transport through Functionalised Carbon Nanotubes: Implications for Desalination Technology. *Energy Environ. Sci.* **2011**, *4*, 751–759.

37. Allen, R.; Hansen, J.-P.; Melchionna, S. Molecular Dynamics Investigation of Water Permeation Through Nanopores. *J. Chem. Phys.* **2003**, *119*, 3905–3919.

38. Beckstein, O.; Sansom, M. S. P. Liquid-Vapor Oscillations of Water in Hydrophobic Nanopores. *Proc. Natl. Acad. Sci. U.S.A.* **2003**, *100*, 7063–7068.

39. Beckstein, O.; Biggin, P. C.; Sansom, M. S. P. A Hydrophobic Gating Mechanism for Nanopores. *J. Phys. Chem. B* **2001**, *105*, 12902–12905.

40. Allen, R.; Melchionna, S.; Hansen, J. Permeation of Nanopores by Water: The Effects of Channel Polarization. *J. Phys.: Condens. Matter* **2003**, *15*, S297–S302.

41. Roth, R.; Gillespie, D.; Nonner, W.; Eisenberg, R. E. Bubbles, Gating, and Anesthetics in Ion Channels. *Biophys. J.* **2008**, *94*, 4282–4298.

42. Blount, P.; Moe, P. C. Bacterial Mechanosensitive Channels: Integrating Physiology, Structure and Function. *Trends Microbiol.* **1999**, *7*, 420–424.

43. Yoshimura, K.; Batiza, A.; Schroeder, M.; Blount, P.; Kung, C. Hydrophilicity of a Single Residue within MscL Correlates with Increased Channel Mechanosensitivity. *Biophys. J.* **1999**, *77*, 1960–1972.

44. Birkner, J. P.; Poolman, B.; Koçer, A. Hydrophobic Gating of Mechanosensitive Channel of Large Conductance Evidenced by Single-Subunit Resolution. *Proc. Natl. Acad. Sci. U.S.A.* **2012**, *109*, 12944–12949.

45. Beckstein, O.; Sansom, M. S. P. A Hydrophobic Gate in an Ion Channel: The Closed State of the Nicotinic Acetylcholine Receptor. *Phys. Biol.* **2006**, *3*, 147–159.

46. Corry, B. An Energy-Efficient Gating Mechanism in the Acetylcholine Receptor Channel Suggested by Molecular and Brownian Dynamics. *Biophys. J.* **2006**, *90*, 799–810.

47. Zhu, F.; Hummer, G. Theory and Simulation of Ion Conduction in the Pentameric GLIC Channel. *J. Chem. Theory Comput.* **2012**, *8*, 3759–3768.

48. Jensen, M. Ø.; Borhani, D. W.; Lindorff-Larsen, K.; Maragakis, P.; Jogini, V.; Eastwood, M. P.; Dror, R. O.; Shaw, D. E. Principles of Conduction and Hydrophobic Gating in K$^+$ Channels. *Proc. Natl. Acad. Sci. U.S.A.* **2010**, *107*, 5833–5838.

49. Aryal, P.; Sansom, M. S. P.; Tucker, S. J. Hydrophobic Gating in Ion Channels. *J. Mol. Biol.* **2014**, 10.1016/j.jmb.2014.07.030.

50. Powell, M. R.; Cleary, L.; Davenport, M.; Shea, K. J.; Siwy, Z. S. Electric-Field-Induced Wetting and Dewetting in Single Hydrophobic Nanopores. *Nat. Nanotechnol.* **2011**, *6*, 798–802.

51. Aryal, P.; Abd-Wahab, F.; Bucci, G. A Hydrophobic Barrier Deep Within the Inner Pore of the TWIK-1 K2P Potassium Channel. *Nat. Commun.* **2014**, *5*, 1–9.

52. Hong, H.; Patel, D. R.; Tamm, L. K.; van den Berg, B. The Outer Membrane Protein OmpW Forms an Eight-Stranded Beta-Barrel with a Hydrophobic Channel. *J. Biol. Chem.* **2006**, *281*, 7568–7577.

53. Hassaine, G.; Deluz, C.; Grasso, L.; Wyss, R.; Tol, M. B.; Hovius, R.; Graff, A.; Stahlberg, H.; Tomizaki, T.; Desmyter, A.; Moreau, C.; Li, X.-D.; Poitevin, F.; Vogel, H.; Nury, H. X-ray Structure of the Mouse Serotonin 5-HT3 Receptor. *Nature* **2014**, *512*, 276–281.

54. Wirth, C.; Condemine, G.; Boiteux, C.; Bernèche, S.; Schirmer, T.; Peneff, C. M. NanC Crystal Structure, a Model for Outer-Membrane Channels of the Acidic Sugar-Specific KdgM Porin Family. *J. Mol. Biol.* **2009**, *394*, 718–731.

55. Song, L.; Hobaugh, M. R.; Shustak, C.; Cheley, S.; Bayley, H.; Gouaux, J. E. Structure of *Staphylococcal* Alpha-Hemolysin, a Heptameric Transmembrane Pore. *Science* **1996**, *274*, 1859–1866.

56. Yamashita, K.; Kawai, Y.; Tanaka, Y.; Hirano, N.; Kaneko, J.; Tomita, N.; Ohta, M.; Kamio, Y.; Yao, M.; Tanaka, I. Crystal Structure of the Octameric Pore of *Staphylococcal* Gamma-Hemolysin Reveals the Beta-Barrel Pore Formation Mechanism by Two Components. *Proc. Natl. Acad. Sci. U.S.A.* **2011**, *108*, 17314–17319.

57. Sansom, M. S. P.; Kerr, I. D. Transbilayer Pores Formed by Beta-Barrels: Molecular Modeling of Pore Structures and Properties Models Investigated. *Biophys. J.* **1995**, *69*, 1334–1343.

58. Šali, A.; Blundell, T. Comparative Protein Modelling by Satisfaction of Spatial Restraints. *J. Mol. Biol.* **1993**, *234*, 779–815.

59. Killian, J. A. Hydrophobic Mismatch between Proteins and Lipids in Membranes. *Biochim. Biophys. Acta* **1998**, *1376*, 401–415.

60. Stansfeld, P. J.; Jefferys, E. E.; Sansom, M. S. P. Multiscale Simulations Reveal Conserved Patterns of Lipid Interactions with Aquaporins. *Structure* **2013**, *21*, 810–819.

61. Cowan, S.; Schirmer, T.; Rummel, G.; Steiert, M. Crystal Structures Explain Functional Properties of Two *E. coli* Porins. *Nature* **1992**, *358*, 727–783.

62. Schirmer, T.; Keller, T. A.; Wang, Y. F.; Rosenbusch, J. P. Structural Basis for Sugar Translocation Through Maltoporin Channels at 3.1 Å Resolution. *Science* **1995**, *267*, 512–514.

63. Biswas, S.; Mohammad, M. M.; Movileanu, L.; van den Berg, B. Crystal Structure of the Outer Membrane Protein OpdK from *Pseudomonas aeruginosa*. *Structure* **2008**, *16*, 1027–1035.

64. Smart, O. S.; Neduvelil, J. G.; Wang, X.; Wallace, B. A.; Sansom, M. S. P. HOLE: A Program for the Analysis of the Pore Dimensions of Ion Channel Structural Models. *J. Mol. Graphics* **1996**, *14*, 354–360.

65. Soares, C. M.; Björkstén, J.; Tapia, O. L3 Loop-Mediated Mechanisms of Pore Closing in Porin: A Molecular Dynamics Perturbation Approach. *Protein Eng.* **1995**, *8*, 5–12.

66. Khalid, S.; Bond, P. J.; Deol, S. S.; Sansom, M. S. P. Modeling and Simulations of a Bacterial Outer Membrane Protein: OprF From *Pseudomonas aeruginosa*. *Proteins* **2006**, *63*, 6–15.

67. Kumar, A.; Hajjar, E.; Ruggerone, P.; Ceccarelli, M. Structural and Dynamical Properties of the Porins OmpF and OmpC: Insights from Molecular Simulations. *J. Phys.: Condens. Matter* **2010**, *22*, 454125.

68. Gravelle, S.; Joly, L.; Detcheverry, F.; Ybert, C.; Cottin-Bizonne, C.; Bocquet, L. Optimizing Water Permeability Through the Hourglass Shape of Aquaporins. *Proc. Natl. Acad. Sci. U.S.A.* **2013**, *110*, 16367–16372.

69. Derrington, I. M.; Butler, T. Z.; Collins, M. D.; Manrao, E.; Pavlenok, M.; Niederweis, M.; Gundlach, J. H. Nanopore DNA Sequencing with MspA. *Proc. Natl. Acad. Sci. U.S.A.* **2010**, *107*, 16060–16065.

70. Borgnia, M.; Nielsen, S. Cellular and Molecular Biology of the Aquaporin Water Channels. *Annu. Rev. Biochem.* **1999**, *68*, 425–458.

71. Beckstein, O.; Tai, K.; Sansom, M. S. P. Not Ions Alone: Barriers to Ion Permeation in Nanopores and Channels. *J. Am. Chem. Soc.* **2004**, *126*, 14694–14695.

72. Allen, T. W.; Andersen, O. S.; Roux, B. Molecular Dynamics—Potential of Mean Force Calculations as a Tool for Understanding Ion Permeation and Selectivity in Narrow Channels. *Biophys. Chem.* **2006**, *124*, 251–267.

73. Zhu, F.; Hummer, G. Drying Transition in the Hydrophobic Gate of the GLIC Channel Blocks Ion Conduction. *Biophys. J.* **2012**, *103*, 219–227.

74. Richards, L. a; Schäfer, A. I.; Richards, B. S.; Corry, B. The Importance of Dehydration in Determining Ion Transport in Narrow Pores. *Small* **2012**, *8*, 1701–1709.

75. Anishkin, A.; Sukharev, S. Water Dynamics and Dewetting Transitions in the Small Mechanosensitive Channel MscS. *Biophys. J.* **2004**, *86*, 2883–2895.

76. Vaitheeswaran, S.; Rasaiah, J. C.; Hummer, G. Electric Field and Temperature Effects on Water in the Narrow Nonpolar Pores of Carbon Nanotubes. *J. Chem. Phys.* **2004**, *121*, 7955–7965.

77. Dzubiella, J.; Allen, R. J.; Hansen, J.-P. Electric Field-Controlled Water Permeation Coupled to Ion Transport through a Nanopore. *J. Chem. Phys.* **2004**, *120*, 5001–5004.

78. Cross, T. A.; Dong, H.; Sharma, M.; Busath, D. D.; Zhou, H.-X. M2 Protein from Influenza A: From Multiple Structures to Biophysical and Functional Insights. *Curr. Opin. Virol.* **2012**, *2*, 128–133.

79. Smirnov, S.; Vlassiouk, I.; Lavrik, N. Voltage-Gated Hydrophobic Nanopores. *ACS Nano* **2011**, *5*, 7453–7461.

80. Kutzner, C.; Grubmüller, H.; de Groot, B. L.; Zachariae, U. Computational Electrophysiology: The Molecular Dynamics of Ion Channel Permeation and Selectivity in Atomistic Detail. *Biophys. J.* **2011**, *101*, 809–817.

81. Shirts, M. R.; Pitera, J. W.; Swope, W. C.; Pande, V. S. Extremely Precise Free Energy Calculations of Amino Acid Side Chain Analogs: Comparison of Common Molecular Mechanics Force Fields for Proteins. *J. Chem. Phys.* **2003**, *119*, 5740–5760.

82. Grossfield, A.; Ren, P.; Ponder, J. W. Ion Solvation Thermodynamics from Simulation with a Polarizable Force Field. *J. Am. Chem. Soc.* **2003**, *125*, 15671–15682.

83. Patel, S.; Davis, J. E.; Bauer, B. A. Exploring Ion Permeation Energetics in Gramicidin A Using Polarizable Charge Equilibration Force Fields. *J. Am. Chem. Soc.* **2009**, *131*, 13890–13891.

84. Bauer, B.; Lucas, T.; Meninger, D.; Patel, S. Water Permeation through DMPC Lipid Bilayers Using Polarizable Charge Equilibration Force Fields. *Chem. Phys. Lett.* **2011**, *508*, 289–294.

85. Bond, P. J.; Sansom, M. S. P. Insertion and Assembly of Membrane Proteins *via* Simulation. *J. Am. Chem. Soc.* **2006**, *128*, 2697–2704.

86. Stansfeld, P. J.; Sansom, M. S. P. From Coarse Grained to Atomistic: A Serial Multiscale Approach to Membrane Protein Simulations. *J. Chem. Theory Comput.* **2011**, *7*, 1157–1166.

87. Berendsen, H.; Spoel, D.; Van Der; Van Drunen, R. GROMACS: A Message-Passing Parallel Molecular Dynamics Implementation. *Comput. Phys. Commun.* **1995**, *91*, 43–56.

88. Hess, B.; Kutzner, C.; Van Der Spoel, D.; Lindahl, E. GROMACS 4: Algorithms for Highly Efficient, Load-Balanced, and Scalable Molecular Simulation. *J. Chem. Theory Comput.* **2008**, *4*, 435–447.

89. Scott, W.; Hünenberger, P.; Tironi, I. G.; Mark, A. E.; Billeter, S. R.; Fennen, J.; Torda, A. E.; Huber, T.; Kruger, P.; van Gunsteren, W. F. The GROMOS Biomolecular Simulation Program Package. *J. Phys. Chem. A* **1999**, *103*, 3596–3607.

90. Oostenbrink, C.; Villa, A.; Mark, A. E.; van Gunsteren, W. F. A Biomolecular Force Field Based on the Free Enthalpy of Hydration and Solvation: The GROMOS Force-Field Parameter Sets 53A5 and 53A6. *J. Comput. Chem.* **2004**, *25*, 1656–1676.

91. Darden, T.; York, D.; Pedersen, L. Particle Mesh Ewald: An $N \cdot$ Log (N) Method for Ewald Sums in Large Systems. *J. Chem. Phys.* **1993**, *98*, 10089–10091.

92. Berendsen, H. The Missing Term in Effective Pair Potentials. *J. Phys. Chem.* **1987**, *91*, 6269–6271.

93. Bussi, G.; Donadio, D.; Parrinello, M. Canonical Sampling through Velocity Rescaling. *J. Chem. Phys.* **2007**, *126*, 014101.

94. Hess, B.; Bekker, H.; Berendsen, H. J. C.; Fraaije, J. G. E. M. LINCS: A Linear Constraint Solver for Molecular Simulations. *J. Comput. Chem.* **1997**, *18*, 1463–1472.

95. Michaud-Agrawal, N.; Denning, E. J.; Woolf, T. B.; Beckstein, O. Software News and Updates MDAnalysis: A Toolkit for the Analysis of Molecular Dynamics Simulations. *J. Comput. Chem.* **2011**, *32*, 2319–2327.

96. Stelzl, L. S.; Fowler, P. W.; Sansom, M. S. P.; Beckstein, O. Flexible Gates Generate Occluded Intermediates in the Transport Cycle of LacY. *J. Mol. Biol.* **2014**, *426*, 735–751.

97. Humphrey, W.; Dalke, A.; Schulten, K. VMD: Visual Molecular Dynamics. *J. Mol. Graphics* **1996**, *14*, 33–38.

98. Grossfield, A. WHAM: The weighted histogram analysis method, version 2.0.9 http://membrane.urmc.rochester.edu/content/wham.